RSC Advances

PAPER

View Article Online
View Journal | View Issue

Cite this: *RSC Adv.*, 2020, **10**, 32309

Facile synthesis of flower-like hierarchical N-doped Nb_2O_5/C nanostructures with efficient photocatalytic activity under visible light†

Fahim A. Qaraah, [a] Samah A. Mahyoub, [b] Abdo Hezam, [c] Wei Zhang,[a] Guangli Xiu, *[a] Janvier Munyaneza[a] and Chengzi Wu[a]

Received 29th March 2020
Accepted 20th July 2020

DOI: 10.1039/d0ra02868a

rsc.li/rsc-advances

Significant endeavors have been devoted in the past few years to establish efficient visible light-activated photocatalysts. Herein, we successfully synthesized a flower-like hierarchical nitrogen-doped and carbon-sensitized Nb_2O_5 (NBO) nanostructure (denoted N-NBO/C). The as-prepared N-NBO/C possessed a specific surface area of 260.37 m^2 g^{-1} and single wire diameter of less than 10 nm. The effect of reaction parameters such as hydrothermal reaction time, temperature and concentration of hexamethylenetetramine (Hmta) on the morphology of NBO was systematically investigated to elucidate the growth mechanism. The carbon on the surface and the nitrogen in the framework of NBO are beneficial for light harvesting, visible light absorption, formation of oxygen vacancies, and electron–hole separation. The photocatalytic performance of the as-fabricated N-NBO/C nanostructures was estimated *via* the photodegradation of 30 mg L^{-1} RhB, where greater than 98% of RhB was decomposed within 30 min upon visible-light radiation. Hence, the obtained N-NBO/C nanostructure exhibits much higher photocatalytic activity for the decomposition of RhB upon visible light irradiation than that of pure niobium oxide (NBO), nitrogen-doped titanium oxide (N-TIO), and nitrogen-doped niobium oxide (N-NBO). This work supplies a versatile route for the synthesis of nitrogen-doped and carbon-sensitized metal-oxide nanostructures for possible utilization in solar energy transformation and environmental remediation.

1 Introduction

In recent decades, there has been a severe drinking water crisis globally due to environmental risks. Besides, existing water supplies are contaminated owing to human activities and the disposal of liquid waste from manufacturing.[1] The prime example of environmental pollutants destroying water resources is organic dyes from various manufacturing industries (such as textiles, paper, and pulp).[2,3] These organic dyes are toxic chemicals that are carcinogenic and mutagenic,[4,5] and can resist bio-decomposition processes.[6] Therefore, their presence in wastewater has become a significant issue for human health and the environment. Although these chemicals are present at a low concentration, they affect aquatic plants and animals and can also affect the function of photosynthesis within the ecosystem. Therefore, low-cost and effective technologies must be established to remove these harmful chemicals from polluted water sources.

Photocatalysis *via* the use of nanostructured semiconductor materials has been reported to be a capable strategy for environmental decontamination.[7–9] Accordingly, nanostructured semiconductor metal-oxides (for instance TiO_2, SnO_2, ZrO_2, and NBO) are the main candidates that have been examined as capable catalytic effective materials for the production of energy and environmental treatment thanks to their well-ordered structure, bandgap and electronic properties.[10] Sunlight irradiation contains around 5% UV-light, 47% visible-light, and 48% infrared radiation. However, metal oxide-based photocatalysts are only photosensitive to ultraviolet light ($\lambda < 400$ nm) because of their broad bandgap. Besides, they suffer from a high (e^-/h^+) pair recombination rate, leading to low photocatalytic activity. Thus, to overcome these two main problems, the surface of metal oxides can be altered using (metal/or non-metal) dopant materials for the efficient breakdown of organic contaminants. C. V. Reddy *et al.*[10–12] found that the presence of metal such as Fe, Mn and Cu in the lattice of zirconium oxide (metal-doped ZrO_2) reduced its bandgap to the visible light region, which promoted the photocatalytic performance in the photodegradation of Rhodamine B. Nevertheless, metal-doped semiconductor metal

[a]*State Environmental Protection Key Lab of Environmental Risk Assessment and Control on Chemical Processes, School of Resources & Environmental Engineering, East China University of Science and Technology, Shanghai 200237, China. E-mail: xiugl@ecust.edu.cn; y10180466@mail.ecust.edu.cn; Tel: +86 18019712552*

[b]*State Key Laboratory of Chemical Engineering, School of Chemical Engineering, East China University of Science and Technology, Shanghai 200237, China*

[c]*Centre for Materials Science and Technology, University of Mysore, Vijana Bhavana, P.B.No. 21, Manasagangothri, Mysore, 570006, India*

† Electronic supplementary information (ESI) available. See DOI: 10.1039/d0ra02868a

oxide photocatalysts can undergo photo-corrosion during the photocatalytic process. Hence, the use of non-metals elements, such as N, C, and S, instead of metallic elements, is an efficient way of enriching photocatalysts and overcoming the above-mentioned problems.[13]

Among the various semiconductors, niobium oxide (NBO) has been widely used in a wide range of applications due to its distinguished physio-chemical characteristics and harmless highly stable, cost-effective and eco-friendly nature.[14–16] However, the photocatalytic efficiency of NBO is restricted to the ultraviolet region due to its large bandgap.[17] Moreover, the rapid recombination rate of its photoexcited charge carriers impedes its photocatalytic efficiency in green applications. Accordingly, N doping has been shown to be effective in ensuring that NBO is receptive to visible light. O atoms are substituted by N atoms, which can decrease the bandgap by mixing N 2p to O 2p orbitals.[18–20] Currently, N-doped NBO photocatalysts have been synthesized using several techniques and different sources of N such as urea,[21] amine,[22] and ammonia.[23] However, the development of 3D N-doped NBO with a high specific surface area is still challenging. Accordingly, the absorption spectrum of NBO nanostructures can be broadened to the visible light region by sensitization with carbon, which acts as a surface sensitizer.[24,25] Consequently, both nitrogen doping and carbon sensitization can mutually enhance the photocatalytic performance of NBO in the visible light region.

Hmta can interact with nanomaterials *via* physical adsorption, electrostatic bonding, and covalent coupling. Moreover, due to its thermolability, Hmta can be easily thermally decomposed into some nitrogen-containing fragments and carbon species.[26] Therefore, Hmta is a potential nitrogen and carbon source for nitrogen doping and carbon decoration, respectively. In addition, it is noteworthy that the morphology and crystal structure of semiconductors play important roles in their photocatalytic behavior because they strongly influence the photoexcited charge separation and transport.[14,15,27] To date, some progress has been achieved in controlling the nanostructures of NBO, such as nanorods,[15] nanowires,[28] nanobelts,[29] nanoplates,[29] nanonets,[25] and nanosheets.[30] More appealingly, their 3D structure with high surface-to-volume ratios, large accessible surface area, excellent permeability, and grain boundaries can provide abundant active sites for adsorbing reactant molecules, diminishing the transfer time of charge carriers and reducing the electron–hole recombination rate.[25,29,31,32] Consequently, it is desirable to prepare 3D NBO nanostructures with a large surface area, N doping, and C sensitization *via* simple and efficient routes.

To the best of our knowledge, the synthesis of flower-like hierarchical N-doped and carbon sensitized NBO using Hmta has not been reported to date. Thus, the aim this study was to fabricate novel flower-like hierarchical N-NBO/C nanostructures through a facile hydrothermal technique followed by calcination. The obtained N-NBO/C possessed a large specific surface area of 260.37 $m^2\ g^{-1}$, small bandgap (2.24 eV) and high N dopant content of 2.45 wt%. The influence of reaction time, concentration of Hmta, and production temperature on the morphology and structure of NBO was explored in detail. In addition, the relation between morphology and photocatalytic efficiency was also discussed. Compared with N-NBO, N-TIO, and pure NBO, N-NBO/C exhibited a much higher photocatalytic performance for the photodegradation of RhB upon visible-light illumination ($\lambda >$ 400 nm). This research will help advance existing efforts in the development of modified semiconductor photocatalysts for efficient operation under visible light.

2 Experimental

2.1. Reagents and chemicals

Niobium oxalate ($C_{10}H_5NbO_{20}\cdot xH_2O$) was obtained from (Shanghai D&B Biological Science and Technology Co., Ltd. Shanghai, China). Hexamethylenetetramine ($C_6H_{12}N_4$), Rhodamine B, ammonium oxalate, benzoquinone, absolute ethanol, urea, and tertiary butanol were obtained from (Shanghai Aladdin Bio-Chem Technology Co., Ltd. Shanghai, China). All chemical reagents were of analytical class and used without further purification.

2.2. Fabrication of flower-like hierarchical NBO nanostructures

The flower-like hierarchical N-NBO/C nanostructures were synthesized using a mild hydrothermal route according to our previous report with slight modifications.[25] Typically, (2 mmol) ($C_{10}H_5NbO_{20}\cdot xH_2O$) was firstly dissolved in 25 mL of mixed solution composed (10 mL) of absolute ethanol and (15 mL) deionized water with agitation at 60 °C to generate solution A, while (0.5 mmol) ($C_6H_{12}N_4$) was suspended in 5 mL deionized water to produce solution B. Solution B was then added dropwise to solution A to create solution C. Subsequently, after agitation for 10 min, solution C was loaded in an autoclave (50 mL) and heated to 180 °C for 12 h. Then, the autoclave was gradually cooled to room temperature and the as-fabricated product was adequately rinsed with deionized water and then dried at 60 °C overnight. The achieved precipitate was designated as NBO-Hmta. Subsequently, the NBO-Hmta precipitate was calcined at 350 °C for 2 h in a muffle furnace. The final product was denoted as N-NBO/C. Furthermore, we optimized some experimental variables, for instance, the Hmta amount (from 5 mmol L^{-1} to 90 mmol L^{-1}), reaction time (1 h, 3 h, 9 h, and 12 h), and reaction temperature (140 °C, 160 °C, 180 °C, and 200 °C) to examine the variation in structural morphology under different reaction conditions in order to achieve the best structure. Finally, the calcination temperature was studied at 150 °C, 250 °C, 350 °C, and 450 °C for 2 h to gain a superior nitrogen-doped and carbon-sensitized NBO nanostructured catalyst. The calcined products at various temperatures were designated as N-NBO/C-x, where x represents the calcination temperature. In contrast, pure Nb_2O_5 (denoted as pure NBO) was fabricated without hexamethylenetetramine, while the other conditions remained the same. Besides, N-doped NBO (N-NBO) and N-doped TiO_2 (N-TIO) were synthesized by calcining a finely milled mixture of commercial NBO (1 g) or commercial TIO (1 g) and urea (3 g) at 400 °C for 3 h.

2.3. Physicochemical characterization

The crystalline structure was characterized *via* powder X-ray diffraction (XRD) with Cu-Kα-radiation in the 2θ range of 10° to 70° on a Rigaku Ultima IV diffractometer. The morphology of the as-prepared catalyst was observed *via* scanning electron microscopy (SEM with a Hitachi S-4800 electron microscope) and transmission electron microscopy (JEM2100F, TEM). The element distribution was also observed through X-ray spectroscopy (EDS). The high-resolution transmission microscopy (HRTEM) images of the samples were obtained on a JEOL JSM-3010 microscope. The structural investigation was performed *via* X-ray photoelectron spectroscopy (XPS), which was achieved with a monochromatic Al-Kα X-ray source ($h\nu$ = 1486.6 eV) on a Kratos Axis Ultra DLD spectrometer. The surface information was also determined using Fourier transform infrared spectroscopy (FT-IR) in the wavenumber range of 400 to 4000 cm^{-1} on a Nicolet-380 FT-IR. N_2 adsorption–desorption isotherms were used to calculate the BET specific surface area and pore size distribution, which were obtained on a Quantachrome Quadrasorb SI apparatus at 77 K. The thermogravimetric and differential thermal analyses were carried out with a Mettler Toledo TGA/DSC 851e instrument from room temperature to 800 °C at a heating rate of 10 °C min^{-1} in air. An Agilent Cary 5000 spectrophotometer was used to analyze the samples in the wavelength range of 200–800 nm, and $BaSO_4$ was selected as a reference. Raman spectra were obtained using an He–Ne laser with a Thermo Fisher Dxr 2Xi spectrometer (l = 633 nm and spot size ≈ 1 mm). Photoluminescence (PL) spectra were measured using a fluorescence spectrophotometer (Jobin Yvon HR 800).

2.4. Evaluations of photocatalysts

The photocatalytic activities of the samples under visible-light were investigated by applying a photocatalytic reactor, as shown in Scheme S1 (see ESI†), to degrade RhB upon irradiation with a 400 W Xe lamp. In a standard process, 200 mg photocatalyst was dispersed in 200 mL aqueous solution of 30 mg L^{-1} RhB in a quartz reactor with a water-cooling jacket. The resulting slurry was agitated for 40 min before being left in the dark to ensure adsorption–desorption equilibrium was achieved between the photocatalyst particles and RhB fragments. In the dark, 3 mL of RhB solution was sampled at 10 min intervals to study the photocatalysis in the dark. Then, an Xe lamp with a UV cutoff filter (400–700 nm) was used to irradiate the slurry under agitation. Subsequently, 3 mL of RhB degradation solution was withdrawn at 5 min intervals and directly centrifuged at 13 500 rpm twice to remove the photocatalyst particle. Then the RhB concentration was recorded using a UV-vis spectrophotometer (UV-2550, Shimadzu).

3 Results and discussion

3.1. Morphology and structure of the photocatalysts

The crystalline properties of the as-prepared N-NBO/C and pure NBO photocatalysts were explored *via* XRD, as shown in Fig. 1(a). The XRD data showed that both samples exhibited four peaks at 22.9°, 26.6°, 46.6°, and 55.4°, corresponding to the (001), (100), (002), and (102) planes, respectively, which can be indexed to pseudo-hexagonal NBO (JCPDS, Card No. 18-0911). No other peaks were observed, indicating the absence of impurities. The strength of the $I(001)/I(100)$ ratio is a benchmark for the oriented degree of NBO nanostructures. Thus, the higher N-NBO/C $I(001)/I(100)$ (19.8) ratio compared to that of pure NBO (14.5) indicates that the growth of the nanostructures was preferentially oriented along the (001) plane in the presence of Hmta during the hydrothermal treatment. Fig. S2(e)† displays that with an increase in the concentration of Hmta (from 15 mmol L^{-1} to 90 mmol L^{-1}), the intensity of the XRD diffraction peaks decreased and shifted significantly due to the increase in the C and N contents. Indeed, the increase in Hmta concentration increased the pH of the solution, and thus we propose that niobium oxalate was destroyed, and accordingly influenced the formation of the nanostructure,[25] which is consistent with the SEM images in Fig. S2(c and d) (see ESI†). Thus, the XRD diffraction in Fig. S2(e)† further confirms that the N-NBO/C nanostructure samples with different nitrogen and carbon contents were obtained by controlling the Hmta concentration.

The intensity of the N and C diffraction peaks was too weak to be observed in the XRD spectra of the N-NBO/C nanostructures, thus Raman spectroscopy was used to verify the existence of C and N in the N-NBO/C structures. As shown in Fig. 1(b), for the pure NBO sample, the broad band positioned at 707.5 cm^{-1} can be attributed to the main Nb–O extension mode; however, for N-NBO/C, the Nb–O extension shaking shifted to 691.5 cm^{-1}, representing the partial symmetry breakage initiated by the introduction of N into the NBO framework.[33] More importantly, the Raman pattern bands corresponding to the carbon species located at 1362 cm^{-1} corresponds to the carbon defect-induced Raman band.[34,35]

The existence of Hmta on the surface of NBO was a crucial parameter in our synthesis route before the calcination treatment to offer a source of C and N elements. Hence, N-NBO/C and NBO-Hmta were analyzed through FT-IR spectroscopy, as shown in Fig. 1(c). The peak at 3344 cm^{-1} is due to the adsorption of H_2O molecules on the sample surface.[24] The peak emerging at 1621 cm^{-1} is due to the hydroxyl group bending vibrations in the H_2O molecules.[25,36] The absorption peaks at 729 cm^{-1} can be ascribed to the angular shaking of Nb–O–Nb and stretching of Nb=O.[25,37] The characteristic absorption bands of Hmta can be observed at 1267 cm^{-1} for the C–N extension vibration,[38] 1718.63 cm^{-1} and 1695.15 cm^{-1} for the extension vibration of the carboxyl group and 3161.82 cm^{-1} for the N–H stretching shaking, indicating that the Hmta molecules are present on the surface of the NBO-Hmta sample. These typical Hmta peaks were not detected for N-NBO/C, indicating that the adsorbed Hmta molecules were almost completely decompose at 350 °C for 3 h during the thermal treatment. Additionally, it is remarkable that the peak located at 1402.40 cm^{-1} indicates the presence of carbonate species (CO_x).[24]

To establish the content of N, C and NBO in the N-NBO/C structures, we examined the TG curve of the as-prepared N-NBO/C (350 °C) structure, as shown in Fig. 1(d). The N-NBO/C

(350 °C) product showed the primary weight loss from around 50 to 300 °C (9.207 wt%) due to the evaporation of surface adsorbed water, gases, and decomposition of amorphous nitrogen and carbon impurities.[34,35] Between 300 °C and 550 °C, weight loss was observed for the N-NBO/C sample, which is ascribed to the decomposition of the remaining nitrogen and carbon content. The weight loss presented in Fig. 1(d) was used to evaluate the weight percentage of nitrogen, carbon and NBO in the N-NBO/C (350 °C) sample. Accordingly, the TGA results imply that the N-NBO/C structures consist of 89.85 wt% NBO and 0.899 wt% of C and N.

The SEM image in Fig. 2(a) obviously displays the as-fabricated N-NBO/C sample clustered into a 3D nanostructure. Upon closer observation of the magnified SEM image in Fig. 2(b), it can be found that the 3D flower nanostructure was woven and built by 1D ultrafine nanowires. Besides, the low and high-magnification TEM Fig. 2(c and d) images, respectively, reveal that the sample was constituted of nanowires, which were aggregated together regularly to form the 3D flower nanostructures.

On the contrary, pure NBO consisted of irregular nanoparticles with an irregular surface (as is evident from Fig. S1(a)) (see ESI†). The TEM image of pure NBO showed that the non-uniform nanoparticles were composed of several collected short nanorods with a diameter of roughly 10 nm Fig S1(b).† Thus, Hmta plays a vital role in the growth of the flower-like hierarchical N-NBO/C nanostructure as a structural-control agent.

The element mapping examination of the N-NBO/C sample is displayed in Fig. 3(b and c), which reveals that the C (red) and N (purple) are uniformly inserted in or dispersed on the photocatalysts. Also, the energy-dispersive X-ray (EDS) investigation illustrated that the major constituents of N-NBO/C are C, N, Nb, and O elements (Fig. S5 and Table S1) (ESI†). The HRTEM image in Fig. 3(f) of a single NBO wire indicates the favored growth of the nanostructure along the (001) direction with a diameter of less than 10 nm. The visible framework fringes are vertical to the nanostructure axis and have a framework gap of roughly 0.37 nm, which correlates perfectly to the *d* value of 0.388 nm obtained from the XRD image in Fig. 1(a). Thus, these results indicate that the presence of Hmta promotes the crystal growth of the NBO nanostructure along the (001) plane.

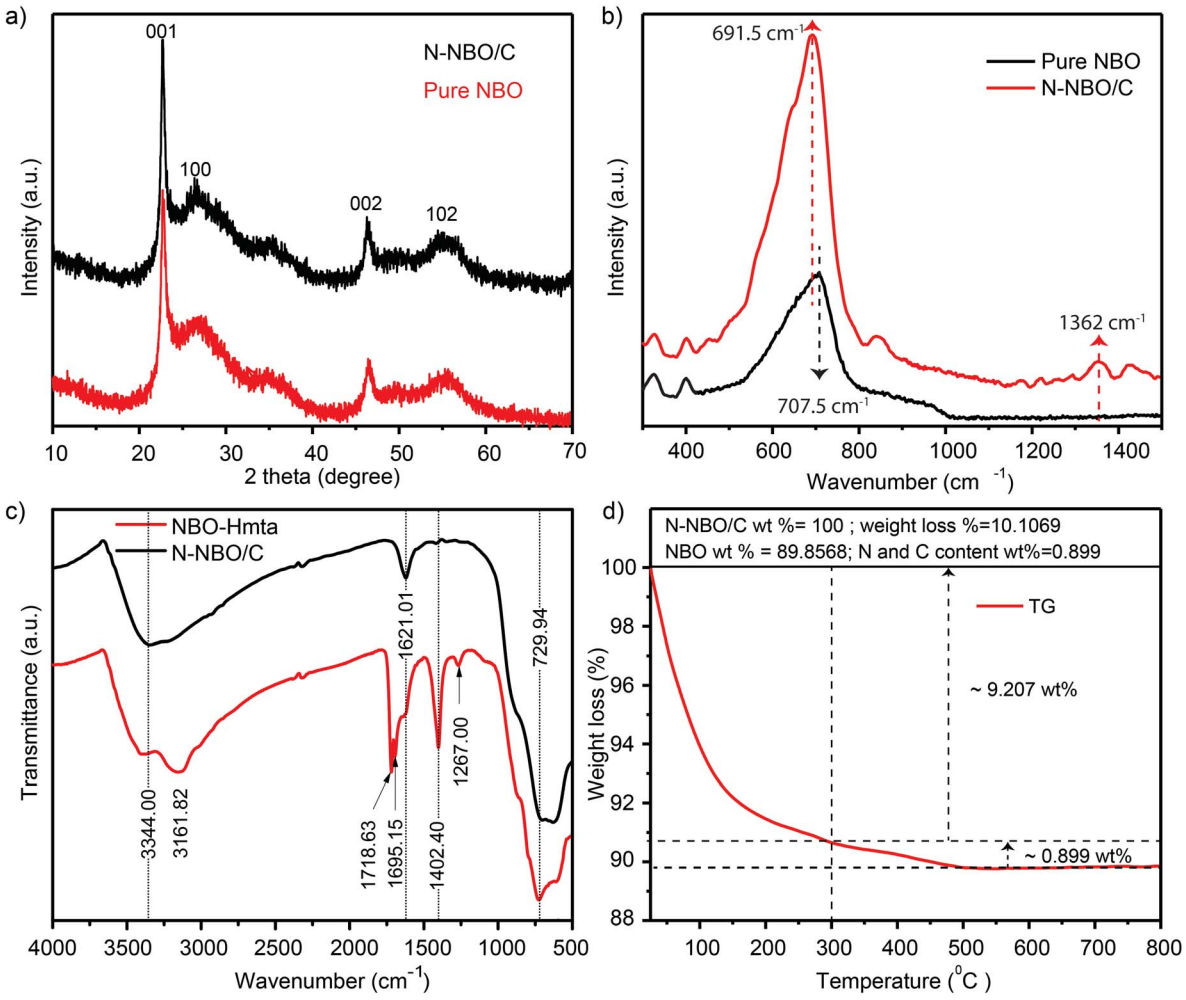

Fig. 1 (a) XRD patterns of N-NBO/C, and pure NBO, (b) Raman spectra of N-NBO/C, and pure NBO, (c) Fourier transform infrared spectra of NBO-Hmta, and N-NBO/C, and (d) TGA curve of N-NBO/C hybrids.

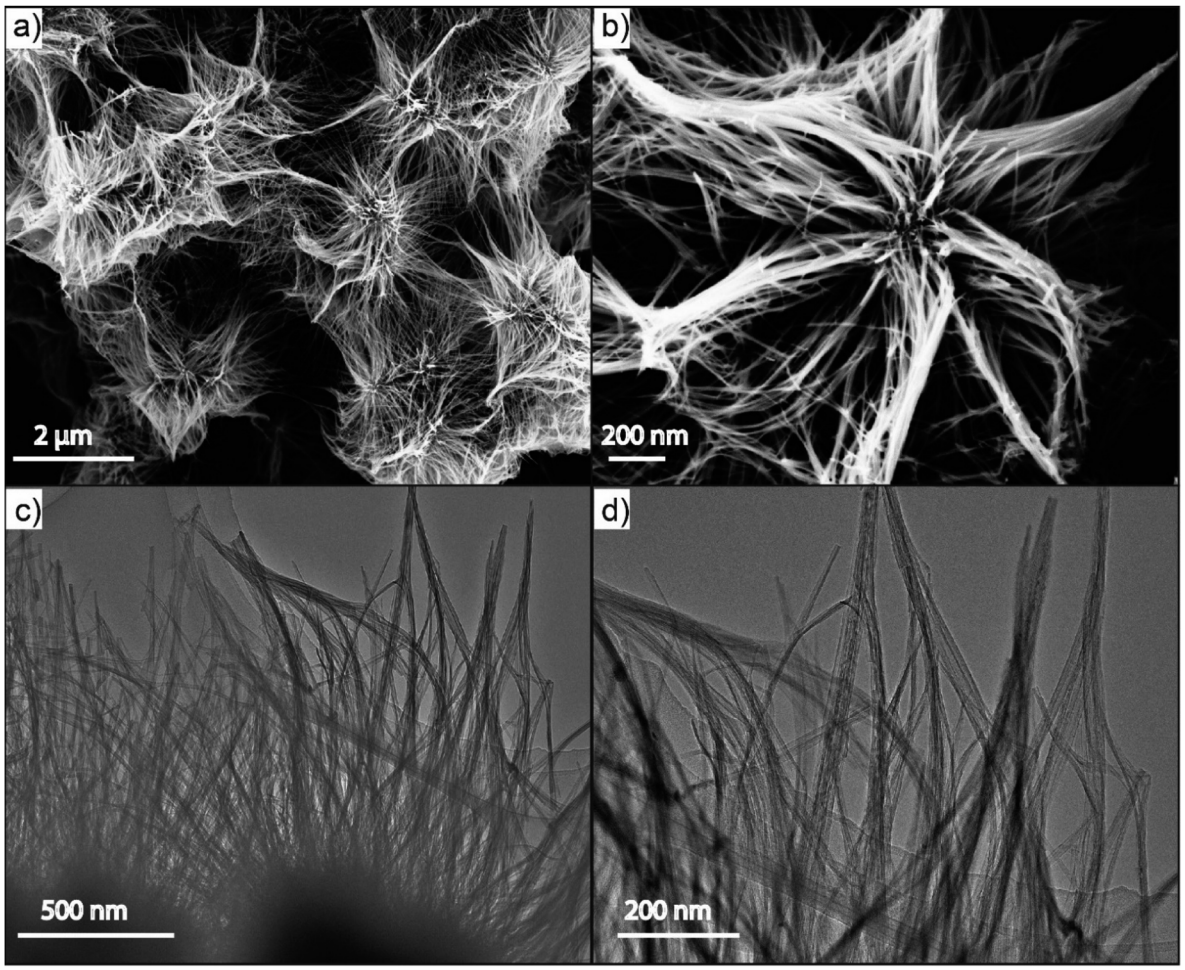

Fig. 2 (a and c) Representative SEM and TEM images, and (b and d) magnified SEM and TEM images of N-NBO/C nanostructures, respectively.

To further examine the porous structure of the flower-like hierarchical N-NBO/C nanostructure, the N_2 adsorption–desorption isotherms and the pore size distribution curve of N-NBO/C are presented in Fig. 4(a and b), respectively. The N-NBO/C surface area is 260.37 $m^2\ g^{-1}$ with a total pore volume of 0.45829 $cm^3\ g^{-1}$ (Table 1), which is obviously the highest among the NBO samples obtained *via* the same preparation method at different calcination temperatures (150 °C, 250 °C, and 450 °C). Mainly, N-NBO/C displays a distinguished pore size distribution of close to 10 nm Fig. 4(b), which provides a tremendous accessible surface for light illumination, more active sites for the adsorption of reactants, and surface hydroxyl groups for capturing photo-generated holes to inhibit the recombination electron–hole pairs.[14,39]

Light consumption and absorption over the catalysts similarly play a critical part in the photocatalytic process.[40] UV-vis diffuse reflectance spectroscopy was utilized to evaluate the band structures of the as-produced Nb-based photocatalysts Fig. 4(c). The sharp absorption edge at *ca.* 400 nm for pure NBO, N-NBO/C (150 °C) and N-NBO/C (450 °C) indicates their insignificant absorption of visible light. Similarly, N-NBO/C (250 °C and 350 °C), N-NBO (400 °C) and N-TIO (400 °C) all absorbed light with a wavelength greater than 400 nm. The estimated bandgaps of the commercial N-NBO, commercial N-TIO, pure NBO, and N-NBO/C (150 °C, 250 °C, 350 °C and 450 °C) are 2.50, 2.86, 3.06, 3.14, 2.83, 2.24 and 3.19 eV, respectively, as shown in Fig. 4(d). On the other hand, N-NBO/C (350 °C) has a smaller bandgap (2.24 eV) and an absorption tail below 500 nm. Based on the XPS results in Fig. 5(e), the O atoms were partially replaced with N atoms in the niobium oxide framework only in N-NBO/C (350 °C). The prolonged absorption spectrum is due to the added electronic states, which are attributed to the N 2p band above the valence band containing mostly O 2p orbitals.[21,41] It is commonly believed that photocatalysis involves light-harvesting over the photocatalyst, the separation and migration of charge carriers, and the use of charge carriers.[31] According to the XPS findings (discussed below), the NO_X, oxygen vacancies, and carbonated species on the as-fabricated Nb-based photocatalysts can play crucial roles in these processes. The oxidized state of N (NO_X species) and carbonated species were noted in N-NBO/C, as shown in Fig. 5(e), which can be beneficial for the transport of charge carriers and increase their lifetime.[25]

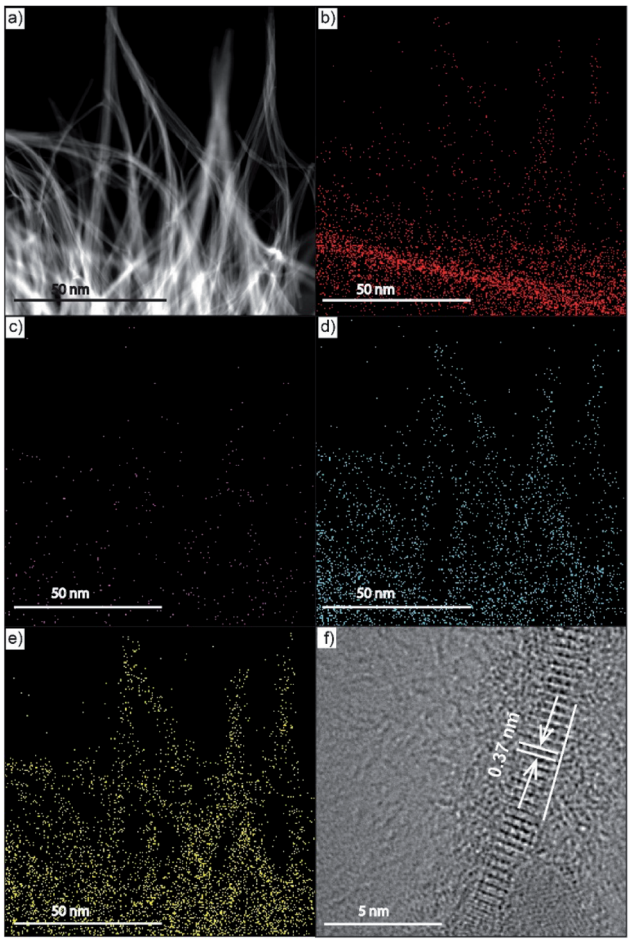

Fig. 3 (a–e) TEM image of as-prepared N-NBO/C and parallel EDS mapping images of C, N, Nb, and O, respectively. (f) HRTEM of the individual single wire N-NBO/C nanostructure.

XPS was employed to analyze the surface chemical composition information of the flower-like hierarchical N-NBO/C nanostructure. As can be seen in Fig. 5(a), for the N-NBO/C nanostructure, there were four elements of 17.79 at% Nb, 60.58 at% O, 2.45 at% N, and 19.19 at% C in the plots. The high-resolution spectra of Nb 3d, which were deconvoluted into two distinguished peaks at 206.6 eV and 209.3 eV, as shown in Fig. 4(b), are ascribed to Nb $3d_{5/2}$ and Nb $3d_{3/2}$, respectively. Nb $3d_{5/2}$ and Nb $3d_{3/2}$ are the representative peaks of the Nb^{5+} ions in NBO.[42] The high-resolution C 1s spectra of the as-fabricated N-NBO/C were deconvoluted into four peaks at 284.2, 284.8, 286 and 288 eV. The two peaks at 284.2 and 284.8 eV are ascribed to adventitious carbon (C–C/C=C),[43] which was created owing to the incomplete burning of the organic constituent and pollution from the air, and the peaks at around 286 eV and 288 eV are ascribed to the existence of C–O and O–C=O groups,[34,35] respectively. The carbon in N-NBO/C is attributed to CO_X species from the incomplete thermal decomposition of the organic component (Hmta) adsorbed on the surface of NBO after the heat treatment. The O 1s spectra were deconvoluted into four peaks at 529.4, 530.1, 530.9, and 531.7 eV, as shown in Fig. 4(d). The two typical peaks at 529.4 and 530.1 eV are ascribed to the Nb–O bond in NBO, and the peaks at around 530.9 eV and 531.7 eV are attributed to the oxygen in the carbonate species and surface adsorbed oxygen O_{ads} (*e.g.*, hydroxyl), respectively.[20,44] Fig. 4(e) depicts the N 1s spectra, where the peaks located at 399.3 eV and 400 eV can be ascribed to chemisorbed N_2 and NO_X species on the surface of NBO.[45] Furthermore, the peaks centered at 394.0 eV and 395.1 eV correspond to the binding energy of the Nb–N bond,[35] corroborating that nitrogen was successfully doped into the NBO lattice.

Photoluminescence analysis is a convenient method to assess the defects and recombination of electron–hole pairs in photocatalysts. Fig. 5(f) presents the PL spectra of N-NBO/C and pure NBO with the maximum peak at about 395 nm, which is assigned to the recombination of electrons and holes in the conduction band and valence band.[33] It can be seen that the N-NBO/C sample shows a lower intensity than that of the pure NBO control sample, revealing the efficient separation of electron–hole pairs in the nitrogen-doped and carbon-sensitized NBO.[40] This can be beneficial for boosting the photocatalytic performance of N-NBO/C.

3.2. Formation mechanism

To examine the evolution of the flower-like hierarchical NBO nanostructures, we first performed time-dependent synthesis and SEM analysis of the products at several steps. Fig. 5(a–d) display the morphological development from non-uniform forms initially to the final flower-like product. No product was obtained at the initial reaction time of 3 h. Upon increasing the reaction time to 9 h, intermediates close to the final morphology were accumulated as nanowires emerged, but some slight distortions were noticed. As the reaction time was prolonged to 12 h, the standard flower-like nanostructures were fabricated. Thus, based on a wide range of experimental observations, it can be concluded that time is one of the significant control aspects in the growth operation.

We similarly explored the influence of the concentration of Hmta on the NBO nanostructure morphology. In the presence of a low amount of Hmta (5 mmol L^{-1}), the products exhibited no ordered forms, as shown in Fig. S2(a) (see ESI†). An increase in the Hmta amount enhanced the production and efficiency of the 3D nanostructure aggregates. As revealed in Fig. S2(b) (see ESI†), when 15 mmol L^{-1} of Hmta was used, flower-like hierarchical NBO aggregates with ordered morphologies and homogenous sizes were obtained. With a continuous increase in the quantity of Hmta in the range of 30 mmol L^{-1} to 60 mmol L^{-1}, the length and size of the nanostructure enlarged gradually and agglomerated to form non-uniform nanostructures, as shown in Fig. S2(c and d) (see ESI†). At excess Hmta concentration, the nanostructures were utterly demolished and agglomerated, as shown in Fig. S2(e) (see ESI†), demonstrating that the presence of Hmta is crucial in the synthesis of the flower-like hierarchical NBO nanostructures as a structural-control agent. Also, an increase in the concentration of Hmta led to an increase in the solution pH. Therefore, niobium oxalate was destroyed, consequently influencing the formation

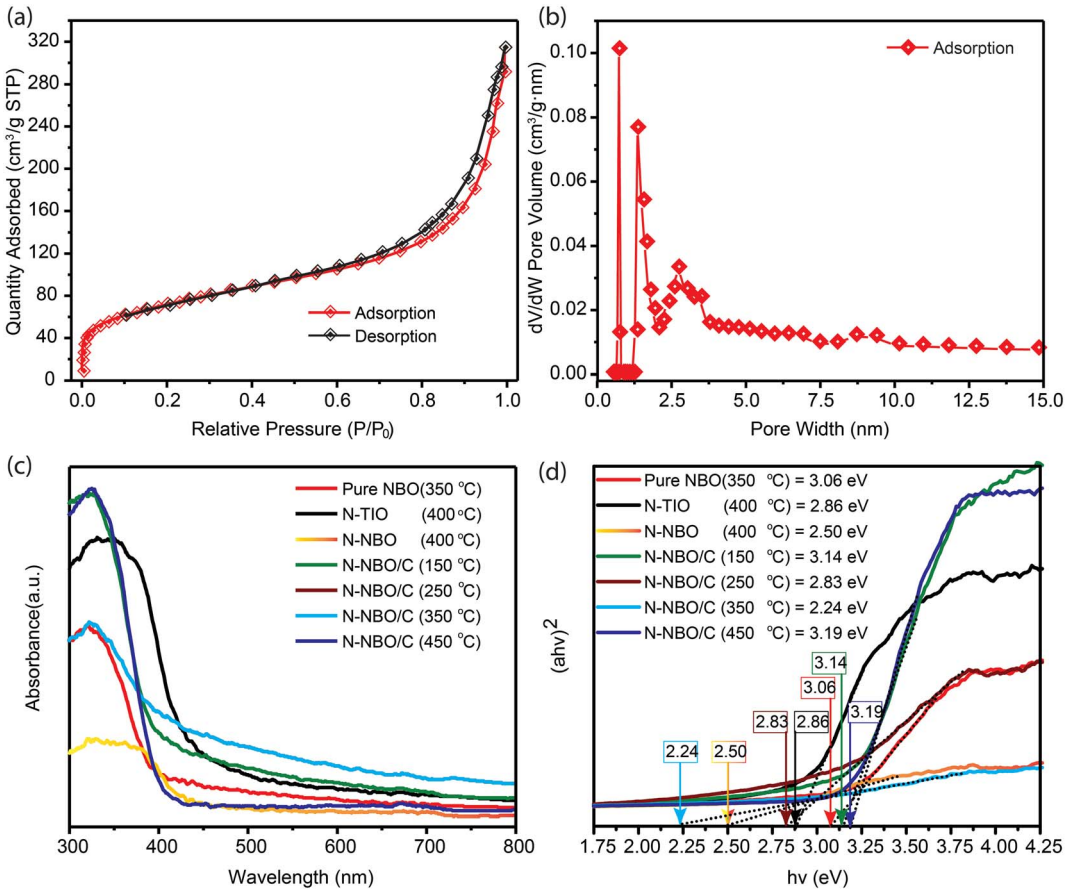

Fig. 4 N_2 adsorption–desorption isotherms of N-NBO/C, (b) pore size distribution curve, (c) UV-vis diffuse reflectance spectra of the as-fabricated N-NBO/C at various calcination temperatures (150 °C, 250 °C, 350 °C and 450 °C) and pure NBO, and (d) plots of $(\alpha h\nu)^2$ *versus* $(h\nu)$.

of the nanostructures.[25] This result matches well with the XRD results in Fig. S2(e) (see ESI†).

On the other hand, we studied the effect of hydrothermal temperature on the final structures of NBO. Elaborate hydrothermal temperature studies were executed, which illustrated that a lower hydrothermal temperature is not favorable for the production of hierarchical NBO nanostructures. The related SEM images are exhibited in Fig. S3(a and b) (see ESI†). We determined that the flower-like hierarchical NBO structures were not observed very clearly at a temperature less than 180 °C, as shown in Fig. S3(c) (see ESI†). Furthermore, hydrothermal treatment at 200 °C caused the flower-like hierarchical NBO structures to be agglomerated into compact nanostructures, as shown in Fig. S3(d) (see ESI†), which is likely due to the decomposition of Hmta at a high temperature.

Based on the abovementioned findings and discussion, we illustrate the possible growth mechanism of the as-prepared NBO nanostructures. In the classical colloidal model, the crystal growth in solution can be classified as either kinetically or thermodynamically regulated, which is subjected to "Ostwald

Table 1 Summary of the physicochemical characteristics, photocatalytic performances, and reaction rate constant, *k*, of N-NBO/C at different calcination temperatures (150 °C, 250 °C, 350 °C, and 450 °C), N-TIO, N-NBO and pure NBO upon visible light illumination

Sample	Surface area ($m^2\ g^{-1}$)	Total pore volume $cm^3\ g^{-1}$	Bandgap (eV)	RhB degradation in 30 min (%)	k (min^{-1})
N-NBO/C (150 °C)	236.87	0.2928	3.14	70.0	0.0336
N-NBO/C (250 °C)	255.05	0.307	2.83	92.3	0.0660
N-NBO/C (350 °C)	260.37	0.4583	2.24	98.5	0.0890
N-NBO/C (450 °C)	165.33	0.2041	3.19	78.6	0.0340
Pure NBO (350 °C)	194.7	0.251	3.06	36.0	0.0293
N-NBO (400 °C)	8.0459	0.01724	2.50	18.0	0.00126
N-TIO (400 °C)	22.9465	0.10003	2.86	20.0	0.00246

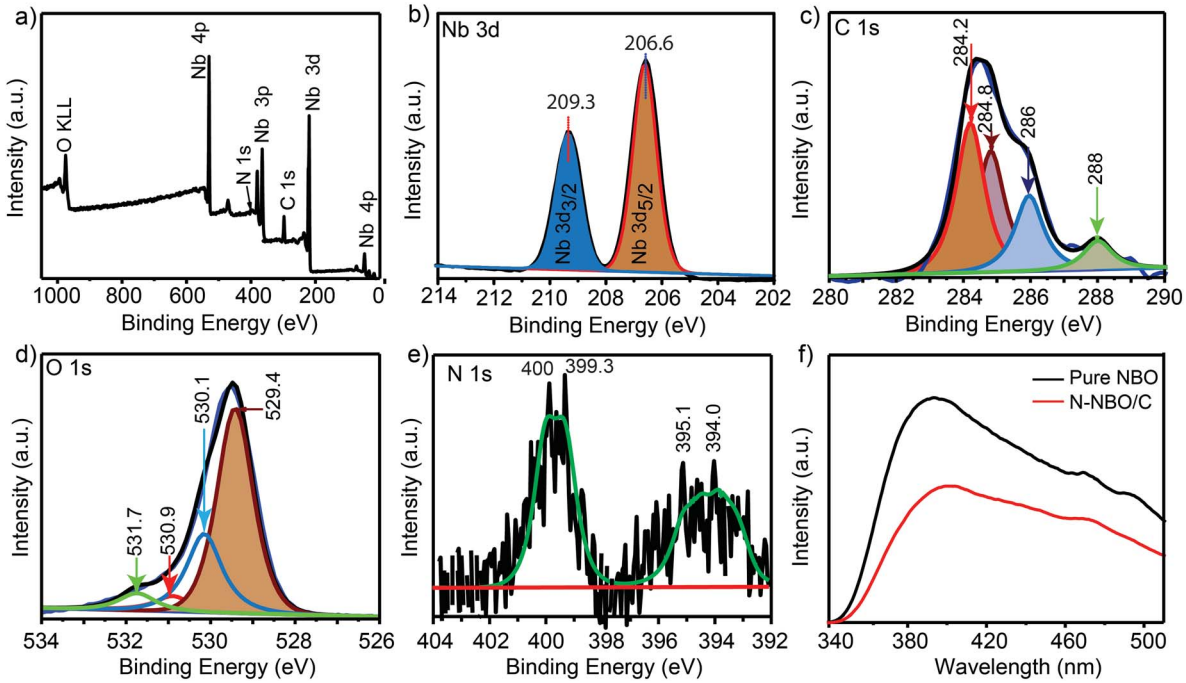

Fig. 5 XPS survey spectrum of N-NBO/C (a), deconvoluted XPS spectra of Nb 3d (b), C 1s (c), O 1s (d), and N 1s (e), and (f) PL spectra of N-NBO/C and pure NBO.

ripening" through the preparation processes. Recently, according to the investigation on fine particles using the hydrothermal technique, a perspective on crystal evolution and oriented attachment appeared.[46–48] In this situation, the driving force for the assembly of particles is still to diminish the total surface energy by removing their higher surface energy faces.[31] Based on the SEM results in our work, we attributed this oriented attachment mechanism to the formation of the 3D flower-like architecture by 1D building blocks. In addition, the anisotropic evolution of the nanostructures in a template-free technique is usually based on the specific surface energies of the equivalent crystal planes. These planes with elevated surface energy have a powerful tendency to collect monomers from the reaction solution, which aggregate to minimize their surface energy.[14] This facilitates the growth along the corresponding planes, finally generating crystals with an anisotropic morphology. Furthermore, the creation mechanism of these novel morphologies requires two steps: (1) nucleation and growth, where the utilization of Hmta as a Lewis base offers weak alkaline conditions,[14] leading to the hydrolysis of niobium oxalate to niobium ionic species $[NbO(OH)_2(C_2O_4)]^-$, which further tends to form $[Nb_2O_4(OH)_2(C_2O_4)_2]^{-2}$ dimeric ionic species.[49] The creation of the dimeric ionic species allows the construction of the crystal nucleus NBO in this weak alkaline state, supplying a driving force for the evolution of the nanoparticles. (2) Self-aggregation by oriented attachment "Ostwald ripening", where adjacent NBO crystal nuclei generated during the first step may be attached to each other and collected into irregular colloidal aggregates to reduce their surface energy and surface area. With the appearance of anisotropic evolution, the irregular assembly may further coagulate to form regular hierarchical 3D nanostructures, which are built by 1D nanowires. Based on the FT-IR results in Fig. 1(c), Hmta can be absorbed on the surfaces of the NBO seeds, leading to a fast growth rate along the (001) orientation than along the (100) orientation. A schematic image of the suggested evolution mechanism of the hierarchical flower-like NBO nanostructures is displayed in Fig. 6(e).

3.3. Calcination temperature effect

The calcination temperature was thoroughly investigated to narrow the photocatalyst bandgap and improve its absorption toward visible-light, which significantly influenced the quantity of N, oxidized state of N, and carbonated species in the catalyst structure directly. Our findings and numerous studies exhibited that the calcination procedure increased the crystallization of the nanoparticles by eradicating the organic remains from the surface of the photocatalysts.[50] Nevertheless, high calcination temperatures can remove all N and C species and lead to the agglomeration of the nanostructures, creating a probable challenge for the optimization of the calcination temperature. At a negligible calcination period of 150 °C, the organic residues were not eradicated from the catalyst surface, as shown in Fig. S4(a) (see ESI†), indicating that increasing the calcination temperature was crucial. As predicted, at 250 °C, a high content of N residue remained on the catalyst. Even though a high content of N residue may remarkably reduce the bandgap, the N acts as recombination centers, resulting in a decrease in the production of free radicals, and thereby low photocatalytic activity.[51] At a calcination temperature of 350 °C, further elimination of N residues from the catalyst was accomplished, and

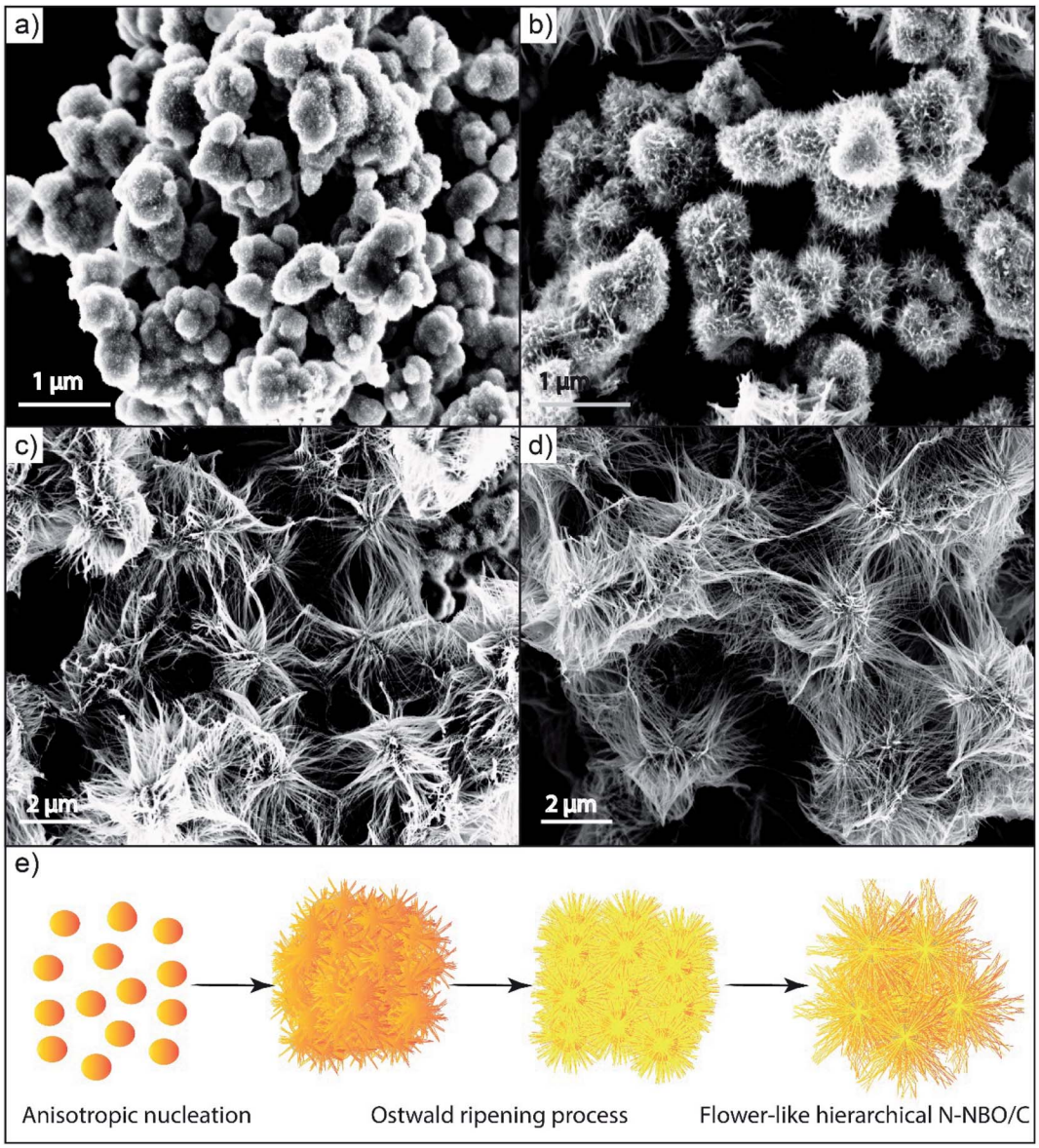

Fig. 6 SEM images of NBO nanostructures fabricated at different reaction stages: (a) 1 h, (b) 3 h, (c) 9 h, and (d) 12 h. (e) Schematic for the formation of the flower-like hierarchical N-NBO/C nanostructures.

the morphology of the nanostructure was improved. When the calcination temperature was increased to 450 °C, the C and N species were eliminated from the photocatalyst, and the nanostructure agglomerated. It must be noted that the quantity of C and N on the as-fabricated catalyst was diminished with an increase in the calcination temperature, and consequently the bandgap was expanded. Thus, we choose the most suitable calcination temperature of 350 °C as the optimal calcination temperature.

4 Photocatalytic performance

The photocatalytic activities for the liquid-phase decomposition of RhB (30 mg L^{-1}) over the as-prepared N-NBO/C nanostructures under visible light were evaluated at a pH of 1.8 at room temperature. Commercial N-NBO, commercial N-TIO, and pure NBO were employed as reference photocatalysts for comparison, and the results are shown in Fig. 7(a). Insignificant photocatalytic degradation of RhB was noted of around 2% after 30 min upon visible-light illumination in the absence of photocatalyst (blue, Fig. 7(a)). However, it was noticeable that the adsorption of N-NBO/C in the dark was approximately 52% RhB, which is significantly greater than that for N-TIO (14%), N-NBO (15%) and pure NBO (15%), as shown in Fig. 7(a). We suppose that this significant adsorption capability in the dark can be ascribed to the C and N sensitization on the surface of the catalyst[52] and its comparatively high specific surface area due to its flower-like nanostructure assemblies, which resulted in high adsorption capability towards RhB in the liquid phase. These results indicate an appropriate photocatalytic reaction. As

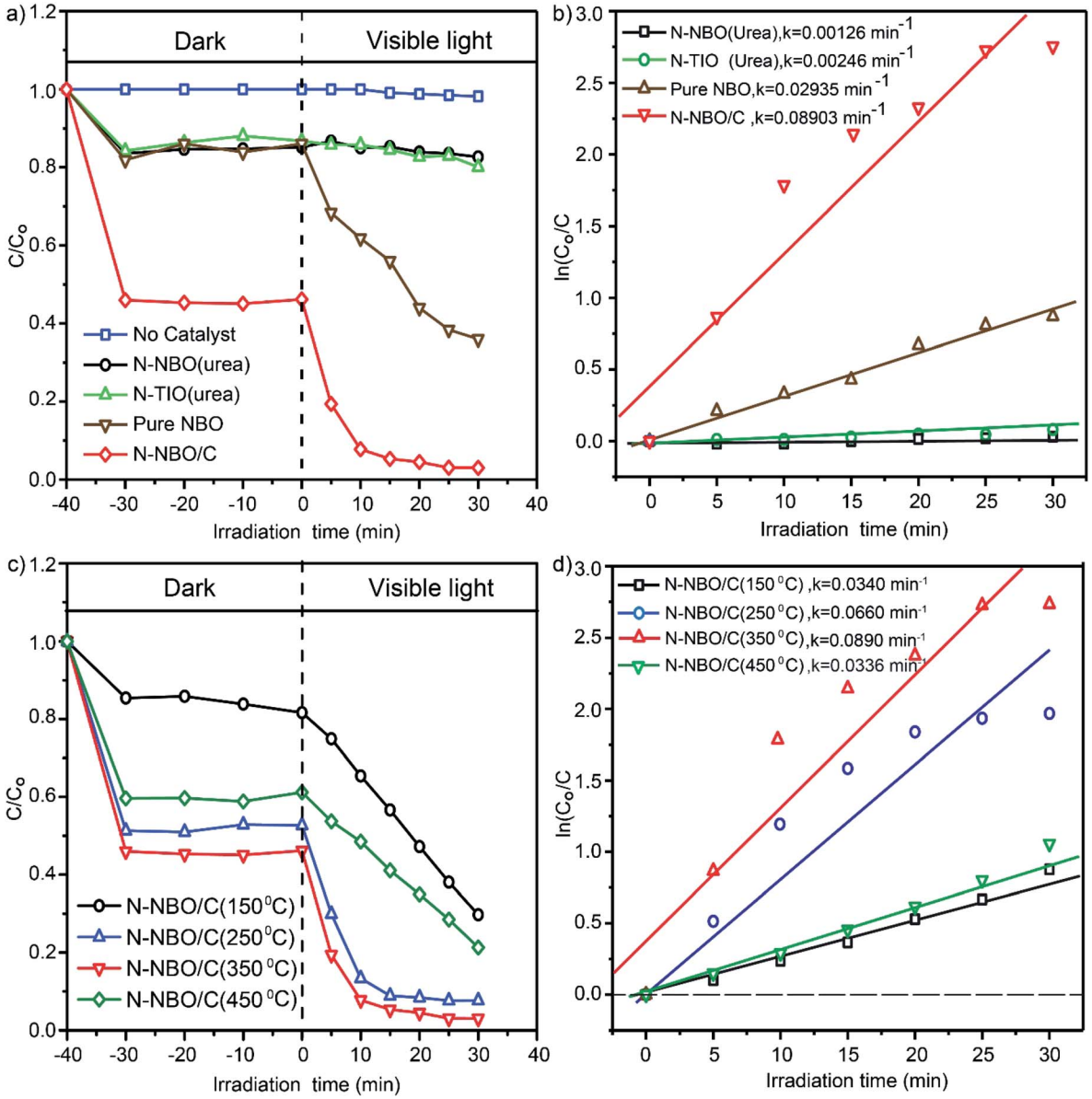

Fig. 7 Time sequence of the decrease in the RhB concentration over N-TIO, N-NBO, pure NBO, and N-NBO/C (a) and fitting curves assuming a pseudo-first-order reaction (b). Photodegradation of RhB by N-NBO/C after calcination at various temperatures (150 °C–450 °C) (c) and fitting curves assuming a pseudo-first-order reaction (d). Data was obtained in 30 mg L^{-1} RhB solution in the presence of 1 g L^{-1} catalyst.

expected, significant photocatalytic activity was observed for N-NBO/C after exposure to light ($\lambda > 400$ nm), which demonstrated a better performance than that for N-TIO and pure NBO. Interestingly, after 30 min of visible light illumination, approximately all of the RhB was decomposed by N-NBO/C. Conversely, N-TIO and N-NBO, which were fabricated using urea, displayed a low photocatalytic performance. Simultaneously, pure NBO only exhibited around 36% photodegradation activity. The highest photocatalytic activity of N-NBO/C can be attributed to several factors including its enhanced visible light absorption, as indicated by the UV-vis results, and large BET surface area/C (260.37 m^2 g^{-1}), which is considerably greater than that of N-TIO, N-NBO, and pure NBO (see Table 1), increasing the number of photocatalytic reaction sites. In general, the three-dimensional (3D) structure of the catalyst can facilitate the flow of reactant molecules and allow them to contact the active sites more efficiently, which leads to a higher photocatalytic performance.[14] Hence, compared with some reported catalysts for the degradation of RhB, this work shows much more significant activity, as shown in Table S2 (see ESI†). Moreover, Fig. S6 (see ESI†) exhibits the absorbance profiles for the degradation of RhB in aqueous solution for the N-NBO/C photocatalyst. With an increase in the irradiation time, the superior absorption peaks of RhB at 554 nm were significantly diminished and shifted to the minimum wavelength in the case of N-NBO/C. This result shows that the RhB solution was almost totally decomposed after irradiation for 30 min, and the aromatic rings and chromophores of RhB were

demolished by N-NBO/C under visible-light illumination[16,53] into aliphatic organic components and slightly mineralized to CO_2 and H_2O.[2,54]

The RhB photocatalytic degradation process fits pseudo-first-order kinetics based on the linear transformation of $\ln(C_0/C) = kt$,[55] where C_0 represents the concentration of RhB molecules after the dark adsorption–desorption equilibrium, and C is the concentration at reaction time t. Fig. 7(b) presents the equivalent fitting results, which suggest that the degradation kinetics generally obeyed the pseudo-first-order reaction. The photocatalytic performance of N-NBO/C was 3.1 times that of pure NBO, 36 times that of N-TIO and approximately 70 times that of N-NBO. These observations are ascribed to the higher specific surface area of the as-prepared catalyst. Besides, nitrogen and carbon played an essential part in promoting its photocatalytic performance.

Our findings also revealed the significance of the calcination temperature, which affected the amount of organic residuals in the photocatalyst with an increase in temperature, producing substantial variations in the performance of our photocatalyst. Fig. 7(c) demonstrates the various results for the photocatalytic decomposition of RhB using N-NBO/C obtained at different calcination temperatures. The results commonly exhibited that all the samples exhibited visible light photocatalytic activity, with the lowest activity for N-NBO/C-450 °C, corresponding to the nearly total removal of C and N, and the superior activity for N-NBO/C-350 °C, further confirming that the optimal calcination temperature was 350 °C. These findings are consistent with the reaction rate constant studies for N-NBO/C at several calcination temperatures, in which the photocatalytic activity of N-NBO/C-350 °C was 2.6, 1.3, and 2.6 times that of N-NBO/C-150 °C, N-NBO/C-250 °C, and N-NBO/C-450 °C, respectively, as shown in Fig. 7(d).

The effect of pH on the photocatalytic decomposition over N-NBO/C was also examined. The experiment was performed at various initial pH of RhB dye (pH 1.8, pH 4.8, pH 8.8 and pH 11.8) (we adjusted the pH solution value using HCl and NaOH). Fig. 8 displays that the highest decomposition of RhB dye (30 mg L^{-1}) occurred at pH 1.8, where RhB was degraded completely by N-NBO/C within 30 min, while that at pH 4.8, pH 8.8 and pH 11.8 was around 90%, 61% and 2%, respectively. In general, the photocatalytic performance is linked with the adsorption efficiency. The point of zero charge (pzc) of NBO is 2.3,[56] and thus it carries a net positive charge at a pH less than its pzc. Consequently, the N-NBO/C photocatalyst displayed excellent photocatalytic performance at a low pH value of 1.8. It is noteworthy that the pKa value for the aromatic carboxyl group present on the RhB molecule is around 4.0. When the pH value of the solution is lower than 4.0, the carboxylic groups on RhB change to the acidic form. Owing to the equilibrium, some carboxylic anions are available in the solution, which are adsorbed on the surface of the catalyst, and then the equilibrium moves to compensate the adsorbed species. This path can be maintained until the full removal of the dye, as shown in Fig. S7(a) (see ESI†). When the solution pH is greater than 4.0, the carboxylic acids group can be ionized and RhB becomes a zwitterion, as shown in Fig. S7(b) (see ESI†).[57] Besides, the

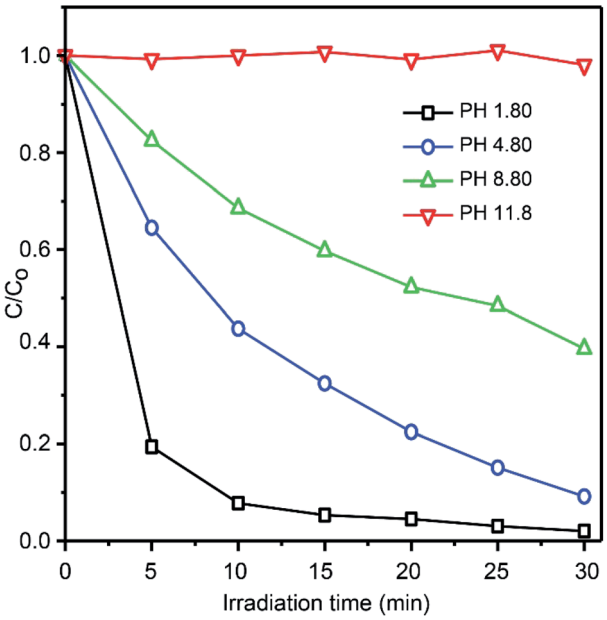

Fig. 8 Photocatalytic degradation of RhB over N-NBO/C nanostructures at various pH values.

zwitterion form of RhB in water may increase the dimerization of RhB because of the appealing electrostatic interactions between the carboxyl and xanthene groups of the monomers. This makes the molecule too big and reduces the charge density by the mutual interactions of two monomers, preventing the removal of RhB.[58,59]

Photocatalyst durability is very significant in the practical applications besides the photocatalytic performance. Consequently, recycling analyses were performed, as presented in Fig. S8 (see ESI†). The flower nanostructure photocatalysts did not show any noteworthy decline in performance for the photodegradation of RhB after five cycles. Based on the analysis of the utilized sample by XRD, as shown in Fig. 9, after the photocatalytic reaction, the crystal structure of the photocatalyst did not change. Hence, this demonstrates that the N-NBO/C nanostructure exhibited durability, which is fundamental to evaluate a photocatalyst and its utilization.

To determine the photocatalytic mechanism for the decomposition of RhB by N-NBO/C, we performed some trapping experiments for numerous active intermediates, including hydroxyl radicals ($^{\bullet}OH$), holes (h^+) and superoxide radical anion ($O_2^{\bullet-}$). The photocatalytic activity of N-NBO/C toward the degradation of RhB with various types of active scavengers is shown in Fig. 10. Ammonium oxalate (AO) is an h^+ scavenger.[60] After the addition of 100 mg AO to the reaction system, the photocatalytic activity decreased considerably, which indicates that holes play a significant role during the photocatalytic process. Benzoquinone (BQ) is a scavenger for $O_2^{\bullet-}$ radicals.[61] According to the results, 1 mg BQ reduced the photodegradation activity of RhB obviously, suggesting that $O_2^{\bullet-}$ radicals play a secondary role in the procedure. However, the photocatalytic performance only decreased slightly upon the addition of 2 mL of tertiary butanol (TBA), a scavenger for $^{\bullet}OH$

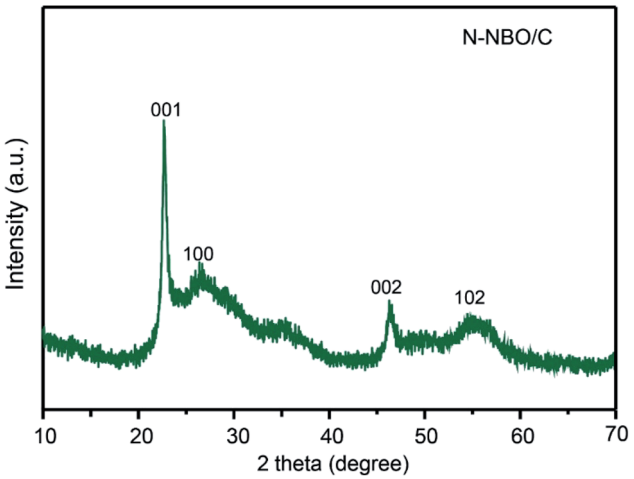

Fig. 9 XRD pattern of N-NBO/C after the photodegradation durability test (5 cycles).

radicals, to the suspension, indicating that ˙OH radicals have a negligible influence on the photodegradation of RhB.

The photocatalytic performance is affected by numerous factors, such as bandgap, crystallinity, and surface properties. Accordingly, for our NBO catalyst, the outstanding photocatalytic achievement can be ascribed to its superior bandgap and structural properties.[62]

A graphic representation of the possible degradation mechanism is presented in Scheme 1. The nitrogen doping leads to an additional level above the valence band of NBO. Moreover, the carbon sensitized on the catalytic surface can drive the generation of h^+ by carbonate species by donating their electrons to the CB of the NBO nanostructure, significantly

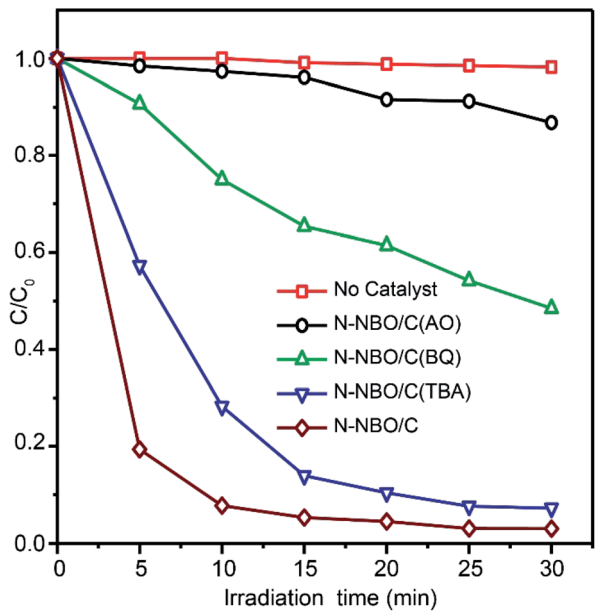

Fig. 10 Photodegradation of RhB by N-NBO/C under various trapping experiment conditions.

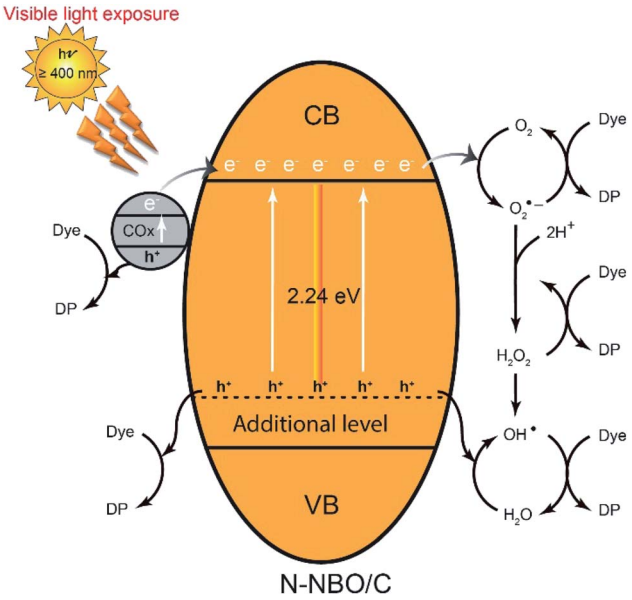

Scheme 1 Mechanism for photodegradation of RhB by N-NBO/C upon visible-light illumination.

indicating that h^+ is an active center for the decomposition of RhB (eqn (1)). Then, the carriers can be captured by oxygen (O_2) and H_2O to form different active species such as $O_2^{\bullet-}$, ˙OH and H_2O_2 (eqn (2)–(5)). Finally, these active species react with the dye molecules directly (eqn (6)).

$$\text{N-NBO/C} + \text{visible light} \rightarrow e_{(Nb_2O_5)}^- + h_{(Nb_2O_5,\ CO_X)}^+ \quad (1)$$

$$O_{2(ads)} + e_{(Nb_2O_5)}^- \rightarrow O_2^{\bullet-} \quad (2)$$

$$O_2^{\bullet-} + 2H^+ \rightarrow H_2O_2 \quad (3)$$

$$H_2O_2 + O_2^{\bullet-} \rightarrow OH^{\bullet} + OH^- + O_2 \quad (4)$$

$$h_{(Nb_2O_5,\ CO_X)}^+ + H_2O \rightarrow H^+ + OH^{\bullet} \quad (5)$$

$$OH^{\bullet},\ h_{(Nb_2O_5,\ CO_X)}^+,\ O_2^{\bullet-} \text{ or } H_2O_2 + \text{dye} \rightarrow \text{degradation product (DP)} \rightarrow H_2O + CO_2 \quad (6)$$

5 Conclusions

In summary, as an efficient visible-light photocatalyst, a flower-like hierarchical nitrogen-doped and carbon-sensitized NBO nanostructure was successfully synthesized *via* a simple hydrothermal-calcination approach based on Hmta as a structure-controlling agent for adjusting the growth of NBO crystals and providing a nitrogen and carbon source. The synergistic effects of N and C on the nanostructure of NBO not only decreased its bandgap significantly from 3.06 to 2.24 eV, but also increased the population of h^+, resulting in a critical improvement in the visible light reaction and substantial photodegradation activity. The best photocatalytic performance of N-NBO/C in our tests for the RhB decomposition upon visible

light illumination is attributed to the mutual contribution of the nitrogen doping and carbon sensitization for extending the light absorption of NBO to the visible region, efficient separation of the electrons and holes, production of abundant oxygen vacancies and high surface area containing accessible active sites. The results from the active species trapping tests indicate that holes play an essential role during the photodegradation of RhB. Meanwhile, $O_2^{\bullet -}$ radicals also play a secondary role in this process.

Conflicts of interest

There are no conflicts declare.

Acknowledgements

This research was financially supported by the National Natural Science Foundation of China (NSFC) (No. 21806037). Fahim A. Qaraah is thankful to Prof. Zhenming Cheng and Dr Yong Wang for their assistance and valuable suggestions.

Notes and references

1 S. P. Dharupaneedi, S. K. Nataraj, M. Nadagouda, K. R. Reddy, S. S. Shukla and T. M. Aminabhavi, *Sep. Purif. Technol.*, 2019, **210**, 850–866.
2 C. V. Reddy, K. R. Reddy, V. V. N. Harish, J. Shim, M. V. Shankar, N. P. Shetti and T. M. Aminabhavi, *Int. J. Hydrogen Energy*, 2020, **45**, 7656–7679.
3 T. Tavangar, M. Karimi, M. Rezakazemi, K. R. Reddy and T. M. Aminabhavi, *Chem. Eng. J.*, 2020, **385**, 123787.
4 S. Dong, J. Feng, M. Fan, Y. Pi, L. Hu, X. Han, M. Liu, J. Sun and J. Sun, *RSC Adv.*, 2015, **5**, 14610–14630.
5 S. Bagheri, A. TermehYousefi and T.-O. Do, *Catal. Sci. Technol.*, 2017, **7**, 4548–4569.
6 Y. Ju, J. Qiao, X. Peng, Z. Xu, J. Fang, S. Yang and C. Sun, *Chem. Eng. J.*, 2013, **221**, 353–362.
7 G. Li, F. Qin, R. Wang, S. Xiao, H. Sun and R. Chen, *J. Colloid Interface Sci.*, 2013, **409**, 43–51.
8 D. Wang, L. Guo, Y. Zhen, L. Yue, G. Xue and F. Fu, *J. Mater. Chem. A*, 2014, **2**, 11716–11727.
9 F. Qin, G. Li, R. Wang, J. Wu, H. Sun and R. Chen, *Chem.–Eur. J.*, 2012, **18**, 16491–16497.
10 C. V. Reddy, I. N. Reddy, V. V. N. Harish, K. R. Reddy, N. P. Shetti, J. Shim and T. M. Aminabhavi, *Chemosphere*, 2020, **239**, 124766.
11 C. V. Reddy, I. N. Reddy, B. Akkinepally, V. V. N. Harish, K. R. Reddy and S. Jaesool, *Ceram. Int.*, 2019, **45**, 15298–15306.
12 C. V. Reddy, I. N. Reddy, K. Ravindranadh, K. R. Reddy, N. P. Shetti, D. Kim, J. Shim and T. M. Aminabhavi, *J. Environ. Manage.*, 2020, **260**, 110088.
13 P. S. Basavarajappa, S. B. Patil, N. Ganganagappa, K. R. Reddy, A. V. Raghu and C. V. Reddy, *Int. J. Hydrogen Energy*, 2020, **45**, 7764–7778.
14 S. Guo, X. Zhang, Z. Zhou, G. Gao and L. Liu, *J. Mater. Chem. A*, 2014, **2**, 9236–9243.
15 P. Hu, D. Hou, Y. Wen, B. Shan, C. Chen, Y. Huang and X. Hu, *Nanoscale*, 2015, **7**, 1963–1969.
16 X. Li, N. Kikugawa and J. Ye, *Adv. Mater.*, 2008, **20**, 3816–3819.
17 Y. Zhao, C. Eley, J. Hu, J. S. Foord, L. Ye, H. He and S. C. E. Tsang, *Angew. Chem., Int. Ed.*, 2012, **51**, 3846–3849.
18 R. Wang, Y. Zhu, Y. Qiu, C.-F. Leung, J. He, G. Liu and T.-C. Lau, *Chem. Eng. J.*, 2013, **226**, 123–130.
19 G. Yang, Z. Jiang, H. Shi, T. Xiao and Z. Yan, *J. Mater. Chem.*, 2010, **20**, 5301.
20 K. Su, H. Liu, B. Zeng, Z. Zhang, N. Luo, Z. Huang, Z. Gao and F. Wang, *ACS Catal.*, 2020, **10**, 1324–1333.
21 H. Huang, C. Wang, J. Huang, X. Wang, Y. Du and P. Yang, *Nanoscale*, 2014, **6**, 7274–7280.
22 M. Qamar, M. Abdalwadoud, M. I. Ahmed, A.-M. Azad, B. Merzougui, S. Bukola, Z. H. Yamani and M. N. Siddiqui, *ACS Appl. Mater. Interfaces*, 2015, **7**, 17954–17962.
23 R. Ullah, H. Sun, H. M. Ang, M. O. Tadé and S. Wang, *Ind. Eng. Chem. Res.*, 2013, **52**, 3320–3328.
24 S. Ge, H. Jia, H. Zhao, Z. Zheng and L. Zhang, *J. Mater. Chem.*, 2010, **20**, 3052.
25 F. A. Qaraah, S. A. Mahyoub, M. E. Hafez and G. Xiu, *RSC Adv.*, 2019, **9**, 39561–39571.
26 S. Chouzier, T. Czeri, M. Roy-Auberger, C. Pichon, C. Geantet, M. Vrinat and P. Afanasiev, *J. Solid State Chem.*, 2011, **184**, 2668–2677.
27 A. Hezam, K. Namratha, Q. A. Drmosh, T. R. Lakshmeesha, S. Srikantaswamy and K. Byrappa, *J. Mater. Sci.: Mater. Electron.*, 2018, **29**, 13551–13560.
28 X. Wang, C. Yan, J. Yan, A. Sumboja and P. S. Lee, *Nano Energy*, 2015, **11**, 765–772.
29 X. Fang, L. Hu, K. Huo, B. Gao, L. Zhao, M. Liao, P. K. Chu, Y. Bando and D. Golberg, *Adv. Funct. Mater.*, 2011, **21**, 3907–3915.
30 W. Fan, Q. Zhang, W. Deng and Y. Wang, *Chem. Mater.*, 2013, **25**, 3277–3287.
31 X. Li, J. Yu and M. Jaroniec, *Chem. Soc. Rev.*, 2016, **45**, 2603–2636.
32 W. Zhao, W. Zhao, G. Zhu, T. Lin, F. Xu and F. Huang, *Dalton Trans.*, 2016, **45**, 3888–3894.
33 A. K. Kulkarni, C. S. Praveen, Y. A. Sethi, R. P. Panmand, S. S. Arbuj, S. D. Naik, A. V. Ghule and B. B. Kale, *Dalton Trans.*, 2017, **46**, 14859–14868.
34 W. Wang, D. Xu, B. Cheng, J. Yu and C. Jiang, *J. Mater. Chem. A*, 2017, **5**, 5020–5029.
35 S. Hemmati, G. Li, X. Wang, Y. Ding, Y. Pei, A. Yu and Z. Chen, *Nano Energy*, 2019, **56**, 118–126.
36 J. Xue, R. Wang, Z. Zhang and S. Qiu, *Dalton Trans.*, 2016, **45**, 16519–16525.
37 G. Liu, L. Zhao, R. Sun, W. Chen, M. Hu, M. Liu, X. Duan and T. Zhang, *Electrochim. Acta*, 2018, **259**, 20–27.
38 A. V. Gerasimova, O. V. Alekhina, L. García-Cruz, J. Iniesta, A. V. Melezhik and A. G. Tkachev, *C*, 2019, **5**, 54.
39 A. S. Cherevan, L. Deilmann, T. Weller, D. Eder and R. Marschall, *ACS Appl. Energy Mater.*, 2018, **1**, 5787–5799.
40 Y. Hong, C. Li, G. Zhang, Y. Meng, B. Yin, Y. Zhao and W. Shi, *Chem. Eng. J.*, 2016, **299**, 74–84.

41 S. Xie, Q. Zhang, G. Liu and Y. Wang, *Chem. Commun.*, 2016, **52**, 35–59.
42 H. Zhang, Y. Wang, P. Liu, S. L. Chou, J. Z. Wang, H. Liu, G. Wang and H. Zhao, *ACS Nano*, 2016, **10**, 507–514.
43 K. Skrodczky, M. M. Antunes, X. Han, S. Santangelo, G. Scholz, A. A. Valente, N. Pinna and P. A. Russo, *Commun. Chem.*, 2019, **2**, 129.
44 Z. Dai, H. Dai, Y. Zhou, D. Liu, G. Duan, W. Cai and Y. Li, *Adv. Mater. Interfaces*, 2015, **2**, 1500167.
45 X. Li, N. Kikugawa and J. Ye, *Chem.–Eur. J.*, 2009, **15**, 3538–3545.
46 J. Liu, X. Huang, Y. Li, K. M. Sulieman, X. He and F. Sun, *Cryst. Growth Des.*, 2006, **6**, 1690–1696.
47 H. Zhu, X. Wang, F. Yang and X. Yang, *Cryst. Growth Des.*, 2008, **8**, 950–956.
48 C. Pacholski, A. Kornowski and H. Weller, *Angew. Chem., Int. Ed.*, 2002, **41**, 1188–1191.
49 J.-M. Jehng and I. E. Wachs, *J. Raman Spectrosc.*, 1991, **22**, 83–89.
50 X. Chen, T. Yu, X. Fan, H. Zhang, Z. Li, J. Ye and Z. Zou, *Appl. Surf. Sci.*, 2007, **253**, 8500–8506.
51 B. Yu, W. M. Lau and J. Yang, *Nanotechnology*, 2013, **24**, 335705.
52 H. Liu, Y. Wu and J. Zhang, *ACS Appl. Mater. Interfaces*, 2011, **3**, 1757–1764.
53 W. Dong, F. Pan, Y. Wang, S. Xiao, K. Wu, G. Q. Xu and W. Chen, *Appl. Surf. Sci.*, 2017, **392**, 514–522.
54 B. T. Huy, C. T. B. Thao, V.-D. Dao, N. T. K. Phuong and Y.-I. Lee, *Adv. Mater. Interfaces*, 2017, **4**, 1700128.
55 Y. Xu, W. Wen and J.-M. Wu, *J. Hazard. Mater.*, 2018, **343**, 285–297.
56 L. A. Rodrigues and M. L. C. P. da Silva, *Desalination*, 2010, **263**, 29–35.
57 A. V Deshpande and U. Kumar, *J. Non-Cryst. Solids*, 2002, **306**, 149–159.
58 A. Ghanadzadeh, M. Zanjanchi and R. Tirbandpay, *J. Mol. Struct.*, 2002, **616**, 167–174.
59 T. Soltani and M. H. Entezari, *Chem. Eng. J.*, 2013, **223**, 145–154.
60 N. Zhang, Y. Zhang, M.-Q. Yang, Z.-R. Tang and Y.-J. Xu, *J. Catal.*, 2013, **299**, 210–221.
61 J. Wang, P. Wang, Y. Cao, J. Chen, W. Li, Y. Shao, Y. Zheng and D. Li, *Appl. Catal., B*, 2013, **136–137**, 94–102.
62 D. Li, X. Duan, Q. Qin, H. Fan and W. Zheng, *J. Mater. Chem. A*, 2013, **1**, 12417.